The magnetically quiet solar surface dominates HARPS-N solar RVs during low activity

Ben S. Lakeland [1]★ Tim Naylor [1], Raphaëlle D. Haywood,[1] Nadège Meunier,[2] Federica Rescigno [1],
Shweta Dalal [1], Annelies Mortier [1],[3] Samantha J. Thompson,[4] Andrew Collier Cameron [1],[5]
Xavier Dumusque,[6] Mercedes López-Morales,[7] Francesco Pepe,[6] Ken Rice [1],[8,9] Alessandro Sozzetti [1],[10]
Stéphane Udry,[6] Eric Ford [1],[11,12,13,14] Adriano Ghedina[15] and Marcello Lodi[15]

[1]*Department of Physics and Astronomy, University of Exeter, Exeter EX4 4QL, UK*
[2]*Univ. Grenoble Alpes, CNRS, IPAG, F-38000 Grenoble, France*
[3]*School of Physics & Astronomy, University of Birmingham, Edgbaston, Birmingham B15 2TT, UK*
[4]*Cavendish Laboratory, JJ Thomson Avenue, Cambridge CB3 0HE, UK*
[5]*Centre for Exoplanet Science/SUPA, School of Physics & Astronomy, University of St Andrews, North Haugh, St Andrews, Fife KY16 9SS, UK*
[6]*Département d'astronomie de l'Université de Genève, Chemin Pegasi 51, CH-1290 Versoix, Switzerland*
[7]*Center for Astrophysics|Harvard & Smithsonian, 60 Garden Street, Cambridge, MA 02138, USA*
[8]*Institute for Astronomy, University of Edinburgh, Royal Observatory, Blackford Hill, Edinburgh EH9 3HJ, UK*
[9]*Centre for Exoplanet Science, University of Edinburgh, Edinburgh EH9 3HJ, UK*
[10]*INAF – Osservatorio Astrofisico di Torino, Via Osservatorio 20, I-10025 Pino Torinese, Italy*
[11]*Department of Astronomy & Astrophysics, Penn State, 525 Davey Laboratory, University Park, PA 16802, USA*
[12]*Center for Exoplanets and Habitable Worlds, Penn State, 525 Davey Laboratory, University Park, PA 16802, USA*
[13]*Institute for Computational and Data Sciences, Penn State, University Park, PA 16802, USA*
[14]*Center for Astrostatistics, Penn State, 525 Davey Laboratory, University Park, PA 16802, USA*
[15]*Fundación Galileo Galilei – INAF – Fundación Canaria, Rambla J. A. Fernández Perez, 7, E-38712 B. Baja (S. C. Tenerife), Spain*

ABSTRACT

Using images from the Helioseismic and Magnetic Imager aboard the *Solar Dynamics Observatory*, we extract the radial velocity (RV) signal arising from the suppression of convective blueshift and from bright faculae and dark sunspots transiting the rotating solar disc. We remove these rotationally modulated magnetic-activity contributions from simultaneous RVs observed by the HARPS-N (High Accuracy Radial velocity Planet Searcher for the Northern hemisphere) solar feed to produce an RV time series arising from the magnetically quiet solar surface (the 'inactive-region RVs'). We find that the level of variability in the inactive-region RVs remains constant over the almost 7-yr baseline and shows no correlation with well-known activity indicators. With an root-mean-square scatter of roughly 1 m s^{-1}, the inactive-region RV time series dominates the total RV variability budget during the decline of solar cycle 24. Finally, we compare the variability amplitude and time-scale of the inactive-region RVs with simulations of supergranulation. We find consistency between the inactive-region RV and simulated time series, indicating that supergranulation is a significant contribution to the overall solar RV variability, and may be the main source of variability towards solar minimum. This work highlights supergranulation as a key barrier to detecting Earth twins.

Key words: methods: data analysis – techniques: radial velocities – Sun: granulation.

1 INTRODUCTION

The radial velocity (RV) method is one of the most valuable tools in the planet hunters' arsenal, as both a detection method, with over 1000 confirmed exoplanets to date, and a vital follow-up tool for transit missions such as the *Kepler* (Borucki et al. 2010), *Transiting Exoplanet Survey Satellite* (Ricker et al. 2014), and upcoming *PLAnetary Transits and Oscillations of stars* (Rauer et al. 2014) missions. Precise RV measurements are often necessary

to independently confirm planetary candidates and to determine planetary masses. As instrumental precision improves, the intrinsic RV variability of the host star becomes the primary obstacle to detecting and characterizing low-mass planets (see Crass et al. 2021, and references therein). Stellar variability can mimic non-existent planets (Rajpaul, Aigrain & Roberts 2016), lead to inaccurate mass measurements (e.g. Blunt et al. 2023; Meunier et al. 2023), or completely obscure the signal of a low-mass planet.

Photospheric magnetic activity primarily causes RV variations via two processes. First, strong magnetic fields act to inhibit convective blueshift of rising stellar material, imparting a net redshift on to the overall stellar RVs (Meunier, Desort & Lagrange 2010a; Dumusque,

★ E-mail: bsl204@exeter.ac.uk

Boisse & Santos 2014). Secondly, bright and dark active regions break the axial symmetry of the rotating stellar disc. This results in an imbalance of flux from the approaching and retreating stellar limbs, causing a net Doppler shift (Saar & Donahue 1997). As these phenomena occur in isolated, magnetically active regions that can persist for multiple rotation cycles, the resulting RV variability typically displays quasi-periodic behaviour with amplitudes of several $m\,s^{-1}$.

Traditional activity mitigation techniques include the use of magnetically sensitive activity indicators that correlate with activity-induced RVs (e.g. Boisse et al. 2011; Haywood et al. 2022), modelling RV variations with Gaussian processes to leverage the quasi-periodicity of isolated active regions rotating with the stellar surface (e.g. Haywood et al. 2014; Rajpaul et al. 2015), and using simultaneous photometry and ancillary time series to estimate the effect of active regions (e.g. Aigrain, Pont & Zucker 2012; Barragán et al. 2022).

While these techniques have proven effective in mitigating the RV variability originating in isolated, magnetically active stellar regions, they do not take into account variability originating from the magnetically quiet stellar surface. Nevertheless, there are a number of phenomena on the quiet stellar surface that can cause RV variability. In particular, observations and simulations of solar convective flows (e.g. granulation and supergranulation) have shown RV variability of the order of 0.5–1 $m\,s^{-1}$ (e.g. Meunier et al. 2015; Meunier & Lagrange 2019, 2020; Al Moulla et al. 2023). In this paper, we use spatially resolved solar images to calculate the RV impact of isolated magnetically active regions (following Meunier, Lagrange & Desort 2010b; Milbourne et al. 2019). We remove these contributions from Sun-as-a-star RVs from the HARPS-N (High Accuracy Radial velocity Planet Searcher for the Northern hemisphere) spectrograph to isolate and directly characterize the RV impact of the magnetically quiet solar surface (hereafter the 'inactive-region RVs').

This paper is structured as follows. In Section 2, we describe the data used in this work and we isolate the inactive-region RVs in Section 3. We analyse the statistical properties of the inactive-region RVs in Section 4 and demonstrate that the inactive-region RVs are not simply an instrumental artefact (Section 5). It is worth noting that, up until this point, our analysis is purely statistical and therefore independent of the physical cause of inactive-region RVs. In Section 6, we show that the inactive-region RVs match simulations of oscillation, granulation, and supergranulation and propose supergranulation as the dominant source of variability. We conclude in Section 7.

2 DATA

2.1 HARPS-N solar telescope

The solar telescope at the Telescopio Nazionale Galileo is a 7.6-cm achromatic lens that feeds the sunlight to an integrating sphere and then into the HARPS-N spectrograph (Dumusque et al. 2015, 2021; Phillips et al. 2016; Collier Cameron et al. 2019). Observations are taken almost continuously during the day time, with 5-min integration times in order to average over the solar p-mode variations. RVs are calculated from the extracted HARPS-N spectra using the HARPS-N data reduction software (DRS; Dumusque et al. 2021). By using the same instrument and DRS used for night-time exoplanet searches, the solar feed provides a realistic Sun-as-a-star RV time series and has yielded information about sub-m s^{-1} level instrumental systematics present in the HARPS-N spectrograph (Collier Cameron et al. 2019). To better emulate night-time stellar observations,

we average three successive observations to give 15-min effective integration times.

In this paper, we use a data set spanning from 2015 July 29 to 2021 November 12. The RVs have been transformed into the heliocentric rest frame, allowing the data to be free of planetary signals. Additionally, a daily differential extinction correction was done following the model described in Collier Cameron et al. (2019). The HARPS-N solar telescope operates continuously, observing from under a plexiglass dome. Data affected by clouds or other bad weather thus need to be accounted for afterwards. To remove potential bad data points, we use two metrics for each observation. First, data quality factor Q is calculated from a mixture model approach described in Collier Cameron et al. (2019). This probability value can be between 0 and 1, where 1 represents the reliable data. Secondly, we extract the maximum and mean count of the exposure meter from the headers of the fits files. The ratio of max and mean, R, should be close to 1 for uniform exposures (and is always higher than 1 by definition). A first quality cut is done using the conditions $Q \geq 0.99$ and $R < 1.5$. From the remaining data points, we fit the histogram of R with a Gaussian function. A slight delay in the shutter opening causes this distribution to resemble a Gaussian, rather than the more expected pile-up around 1. In a second cut, we remove data where R is higher than three standard deviations above the mean. Finally, as a last cut, we perform a 5σ clipping on the remaining RVs. The cuts made are very strict and may indeed remove reliable data too, but it is done to ensure the very high quality of data. The remaining data set has 20 435 observations.

2.2 *SDO*/HMI

The Helioseismic and Magnetic Imager aboard the *Solar Dynamics Observatory* (*SDO*/HMI) uses six narrow bands around the magnetically sensitive 6173 Å Fe I line. A Gaussian fit of the narrow-band fluxes as a function of wavelength is used to derive continuum intensitygrams, magnetograms, and line-of-sight velocity maps (Dopplergrams), each spatially resolved with approximately 1-arcsec resolution. In this work, we use 720-s exposures, every 4 h from 2015 July 29 to 2021 November 12, totalling 12 434 sets of images. We briefly describe how we calculate RVs from these images. For more details, we refer the reader to Haywood et al. (2016) and Milbourne et al. (2019), who describe in detail the process of extracting disc-averaged physical observables from *SDO*/HMI images.

Owing to poor long-term stability of the *SDO*/HMI instrument, we are not able to directly calculate the solar RVs by simply intensity-weighting the Dopplergram pixels. Fig. 2 of Haywood et al. (2022) shows the effects of long-term systematics when calculating the RVs in this way. There are clear jumps in the RVs caused by instrumental effects. This means that we cannot use the Dopplergram to produce long-baseline Sun-as-a-star RV measurements. To overcome this instrumental limitation, we use a physically motivated model to estimate the RV variations arising from two processes on the Sun. In doing so, we calculate the RV variability relative to the quiet Sun (Meunier et al. 2010b; Haywood et al. 2016, 2022; Milbourne et al. 2019).

The first of these is a photometric shift, δRV_{phot}, caused by a bright plage or dark sunspot breaking the rotational symmetry of the solar disc. In the absence of inhomogeneities on the solar disc, the contributions of the blueshifted approaching limb and redshifted retreating limb are in balance, with no overall effect on the solar RVs. If a dark or bright region is present on one of the limbs, the Doppler contribution from that limb is diminished or enhanced,

respectively, resulting in an overall RV shift. The second component, δRV_{conv}, arises from regions with large magnetic flux suppressing convection on the surface of the Sun. The reduction in the convective blueshift in these regions imposes a net redshift on to the overall solar RV. By applying continuum intensity and magnetic flux thresholds described by Haywood et al. (2016), respectively, we isolate the RV contribution of active regions on the Sun.

Since *SDO*/HMI derives its RVs from a single iron line, as opposed to a whole spectrum, Haywood et al. (2016) and Milbourne et al. (2019) fit a linear combination of these components to solar RVs from HARPS and HARPS-N, respectively, to account for the different scaling of each component. They found that δRV_{conv} is the dominant of these two effects in the Sun. Milbourne et al. (2019) only consider the RV contributions from active regions larger than 20 μHem. Those authors find that this cut-off obviates the need to vary the relative contributions of the photometric and convective effects over time. Owing to the fact that the two components forming this RV series are driven by magnetic processes, and that RVs are calculated relative to the quiet Sun, we will refer to the RV series derived from the *SDO*/HMI images as the 'magnetic-activity' RVs. Since the formal uncertainties on the magnetic-activity RVs are significantly lower than the uncertainties for the HARPS-N RVs (Haywood et al. 2022), we will refrain from extensive error analysis of the magnetic-activity RVs.

3 ISOLATING RV CONTRIBUTIONS FROM MAGNETICALLY INACTIVE REGIONS

In this paper, we are interested in the RV variability originating from magnetically quiet regions of the solar surface. To isolate these contributions, we subtract the *SDO*/HMI RVs (which are only sensitive to large magnetically active regions) from the HARPS-N RVs (which probe the entire solar disc). The resultant time series of residual RVs therefore probes the RV signals not arising from the large, magnetically active regions identified by Milbourne et al. (2019). Throughout this paper, we will refer to this time series as the inactive-region RVs. To account for the difference in cadence of *SDO*/HMI and HARPS-N, we interpolate the magnetic-activity RVs on to the HARPS-N timestamps. In principle, this could introduce a signal into the inactive-region RVs, since we are smoothing over all variability in the magnetic-activity RVs over time-scales shorter than 4 h. Recalling, however, that the magnetic-activity RVs encode variability occurring on rotational time-scales, and noting that shorter time-scale processes (e.g. oscillations/granular flows) do not contribute to the magnetic-activity RVs, we are justified in this approach. We provide a quantitative justification in Appendix A. It is worth highlighting that the model of Milbourne et al. (2019), which we use in this paper, does not include the effect of the smallest active regions. However, those authors show that by only considering the largest active regions, they reproduce the majority of the rotationally modulated, activity-induced RVs, without having to introduce an arbitrary trend. The models of Milbourne et al. (2019) reduce the HARPS-N RV scatter from 1.65 to 1.21 and 1.18 m s^{-1} with and without the 20-μHem active-region cut-off, respectively.[1] We are therefore justified in describing the RV time series produced by removing this contribution from the disc-integrated HARPS-N RVs as the 'inactive-region' RVs. We do note, however, that there will

inevitably remain a small component in the inactive-region RVs that corresponds to the smallest scale magnetic regions.

To avoid any effects of long-term instrumental effects, we detrend the inactive-region RVs with a 100-d rolling mean, following the treatment of Al Moulla et al. (2023). We note that such a detrending preserves both the amplitude and time-scale of any short-term variability present in the RV time series, and so will not affect the results of this work. We opt to smooth the inactive-region RVs, as opposed to the HARPS-N RVs, since we are interested in the difference between the RVs measured by HARPS-N and those derived from *SDO*/HMI images. Directly smoothing the HARPS-N RVs would risk smoothing over the rotationally modulated activity signal present in both series, thereby imposing an artificial signal in the residuals when we subtract the unsmoothed magnetic-activity RVs.

Fig. 1 shows the correlation between the daily mean RV and both $\log R'_{HK}$ and unsigned magnetic flux (Haywood et al. 2022) values for the HARPS-N RVs and the inactive-region RVs, as well as the respective Pearson correlation coefficients. We see an almost total removal of any correlation between the RVs and the activity indices when the magnetic-activity RVs are subtracted from the HARPS-N RVs, indicating that we are successfully removing the majority of the RV signal caused by magnetic activity.

In addition, following Al Moulla et al. (2023), we calculate the velocity power spectrum (PS) of the HARPS-N RVs and the residual RVs as follows. Each RV time series can be represented as a linear combination of sinusoidal components:

$$RV(t) = c + \sum_\nu a(\nu) \cos(2\pi\nu t) + b(\nu) \sin(2\pi\nu t),\tag{1}$$

where $a(\nu)$ and $b(\nu)$ are frequency-dependent coefficients, and c is a constant offset. The velocity PS is defined as

$$PS(\nu) = a(\nu)^2 + b(\nu)^2,\tag{2}$$

and is converted to velocity power spectral densities (PSDs) by multiplying by the effective length of the observing window (Kjeldsen et al. 2005).

Fig. 2 shows the two PSDs as well as the ratio of power in the HARPS-N RVs to the inactive-region RVs, calculated for logarithmically spaced bins in frequency. We see evidence of decreased power in the inactive-region RVs at time-scales comparable to and longer than the solar rotation period, whereas the two PSDs are similar for shorter time-scales. This further suggests that we are successful at removing most of the rotationally modulated variability, while retaining the short-time-scale variability characteristics of the HARPS-N RVs.

4 INACTIVE-REGION RVS EXHIBIT A CONSTANT LEVEL OF VARIABILITY

Having established that we are successful in removing the RV signature of large magnetically active regions (Section 3), we now analyse the inactive-region RVs. To investigate how the inactive regions vary throughout the solar cycle, we compare the root-mean-square scatter (RMS) of the RVs with the mean sunspot number, taken from SILSO World Data Center (2023), for 45 50-d intervals, as a proxy for overall activity level. In Fig. 3, we show that there is no correlation. Additionally, despite the sunspot number changing by more than two orders of magnitude, the standard deviations of the RVs vary only slightly. This shows that the inactive-region RV variability remains relatively constant at a wide range of magnetic-activity levels. In Appendix B, we show that the 17 per cent scatter in the RMS shown here is consistent with being dominated by sampling noise.

---

[1]To reduce the RV scatter to 1.18 m s^{-1} when taking into account all active regions, an arbitrary linear drift was introduced. Without that drift, the scatter is reduced to 1.31 m s^{-1}.
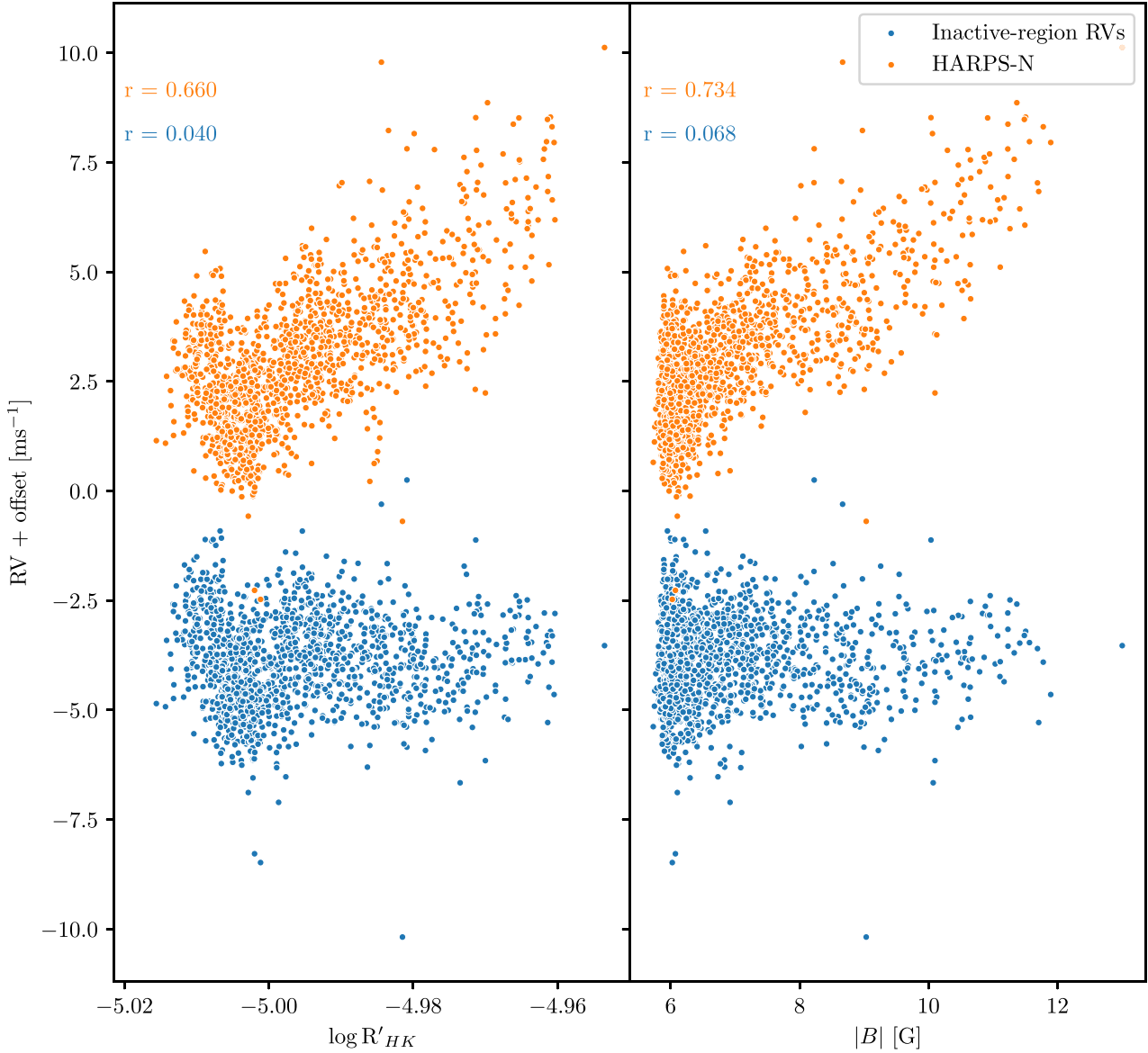
Figure 1. Scatter plots showing the correlation between daily mean RVs (orange for the HARPS-N RVs and blue for the inactive-region RVs) and log R'_{HK} (left) and unsigned magnetic flux (right). Both scatter plots demonstrate an almost complete removal of any correlation between the RVs and the respective activity indicator after subtracting the magnetic-activity RVs. For each data set, we also numerically show the Pearson correlation coefficient. RV data are shown with an offset for clarity.

To investigate how the inactive-region RVs behave at different time-scales, we use structure functions (SFs; see e.g. Simonetti, Cordes & Heeschen 1985; Sergison et al. 2020; Lakeland & Naylor 2022). SFs quantify how the variability within a time series changes with time-scale. In Appendix C1, we show that, for a continuous, uncorrelated signal, the SF is equivalent to

$$SF(\tau) = 2\sigma^2, \tag{3}$$

where σ is the RMS of the signal. We therefore choose to use $\sqrt{\frac{1}{2}SF}$ to quantify the RV variability at a given time-scale τ, emphasizing the connection with the RMS. We provide a more in-depth description of SFs and their key properties required for this analysis in Appendix C.

We now segment the RVs by calendar year and show the corresponding SFs in Fig. 4. We opt to use longer sub-series than the 50-d

samples in Fig. 3 to ensure that each time-scale is well sampled, with many pairs of data points contributing to the calculation for each time-scale. We see that despite covering a wide range of magnetic-activity levels, the inactive-region RVs have similar variability at all time-scales. We also note that, for each 1-yr segment, there is no significant increase in variability at time-scales longer than ~3 d. The typical year-to-year variation is 5–10 per cent. This is comparable to the typical lower-bound sampling error we estimate in Appendix C2, indicating that the true year-to-year variation is very low.

We contrast this with the behaviour of the magnetic-activity RVs over the same baseline. We calculate SFs of the magnetic-activity RVs (again segmented by calendar year). We plot SFs calculated from both the inactive-region RVs and magnetic-activity RVs on the same axis scales in Fig. 5 to highlight the contrast. While the magnetic-activity RVs vary by more than an order of magnitude, the
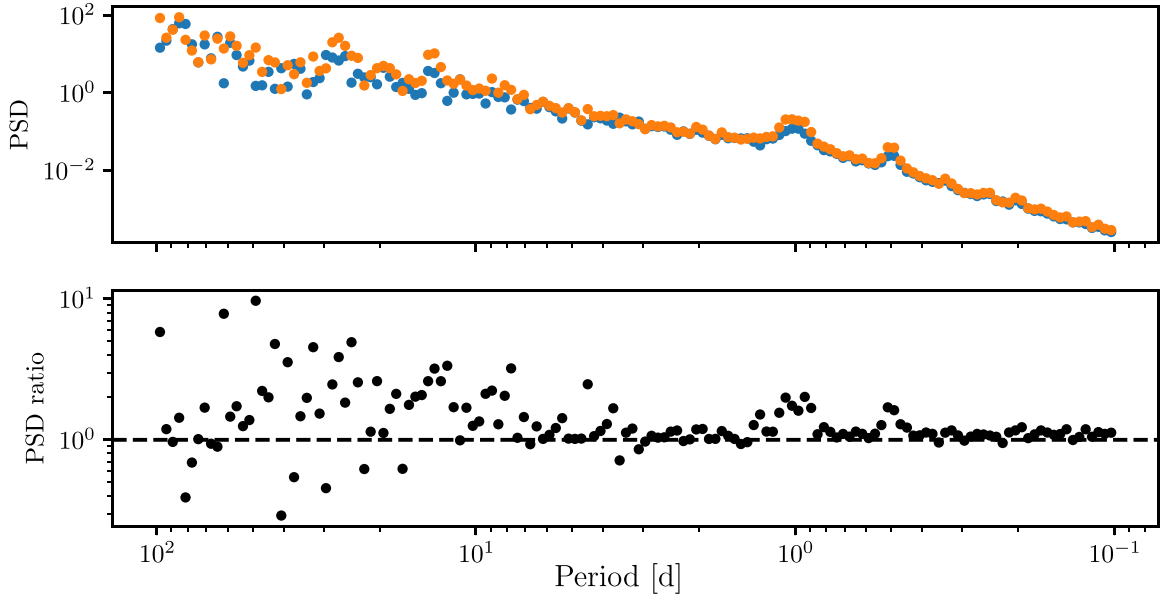
Figure 2. (Top) The PSD of HARPS-N RVs (orange) and of the inactive-region RVs (blue), calculated in 150 logarithmically spaced bins in frequency. (Bottom) The ratio of HARPS-N RV PSD to inactive-region RV PSD. Although there is still a noticeable feature in the residual RV PSD at the rotation period, and at 1 d and its alias, we see lower power at time-scales longer than ~10 d when compared to the full HARPS-N RVs. By contrast, the two PSDs are very similar at shorter time-scales. This indicates that we are successful in removing much of the variability at time-scales around or above the solar rotation period, but we leave the shorter time-scale variability largely unaffected.
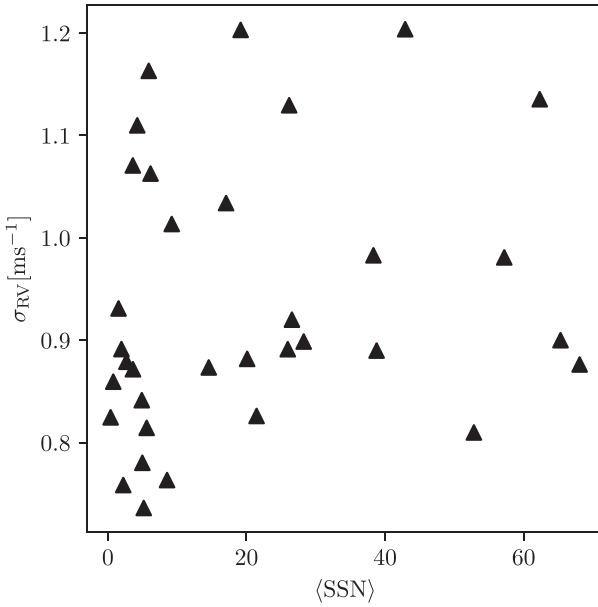
Figure 3. Scatter plot of the mean sunspot number and the standard deviation of inactive-region RV, calculated for non-overlapping 50-d periods from 2015 to 2021. We see no correlation between RV RMS and mean sunspot number.

Figure 4. SFs of inactive-region RVs, divided by calendar year. The lines are coloured by average sunspot number in that year. Despite data collection spanning a wide range of magnetic-activity levels, the variability spectrum for the inactive-region RV shows no significant variation from year to year. The black dashed line shows the SF for the entire inactive-region RV series. We note the gap at $\tau \sim 0.5$ d. This is typical of ground-based telescopes, which cannot observe the Sun at night time.

inactive-region RVs exhibit an almost unchanging level of variability. Fig. 5 also demonstrates that, for the majority of the 7-yr baseline, the variability in the residual RVs is comparable to or larger than the variability shown in the magnetic-activity RVs. This shows that, for the quieter period of solar cycle 24, the majority of the RV variability originated from magnetically inactive regions, as opposed to magnetically active regions. The two contributions are
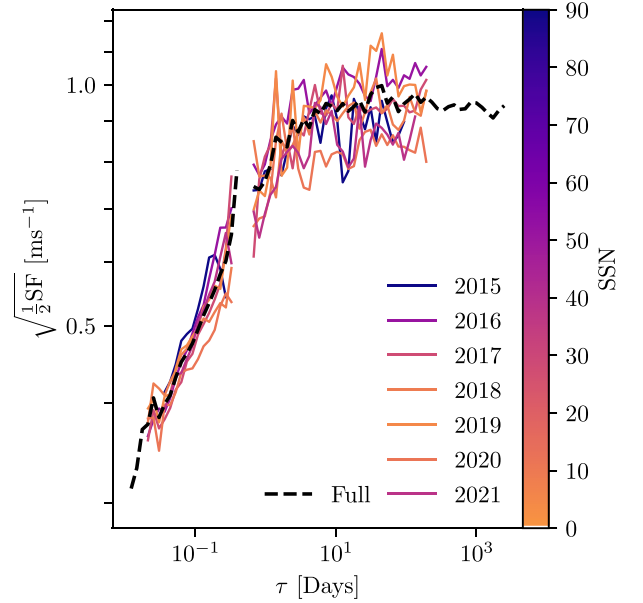
approximately equal during the 2016–2017 period, where the average sunspot number was 39.8. Fig. 6 shows the distribution of yearly averaged sunspot numbers, dating back to 1700 from the World Data Center SILSO, Royal Observatory of Belgium, Brussels (SILSO
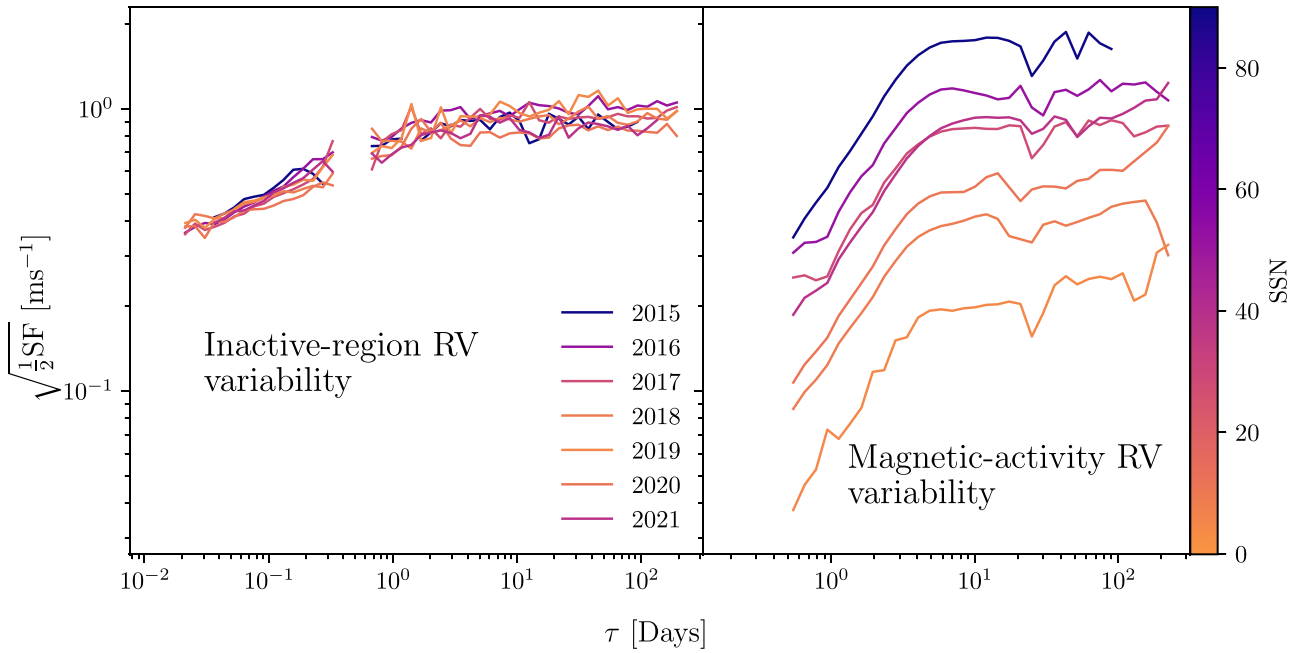
Figure 5. (Left) The SFs shown in Fig. 4 of inactive-region RVs. (Right) The SFs of the corresponding year-long run of magnetic-activity RVs. To illustrate the relative level of variability in the inactive-region and magnetic-activity RVs, both sets of SFs are shown on the same scale. The inactive-region RVs consistently show a level of variability around 1 m s^{-1}. The relatively constant level of variability in the inactive-region RVs contrasts drastically to the large range of variability levels demonstrated in the magnetic-activity RVs. Additionally, the level of variability shown by the inactive-region RVs is often much larger than that in the magnetic-activity RVs. As in Fig. 4, both sets of SFs are coloured by the average sunspot number during the calendar year in which the RVs were obtained.
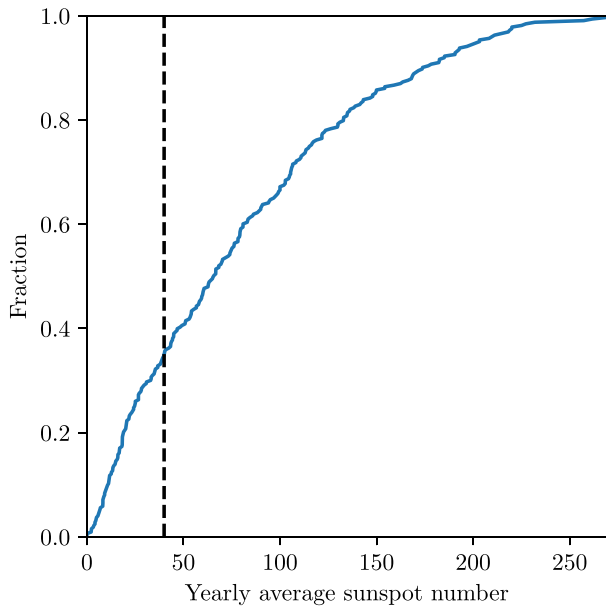
Figure 6. Cumulative distribution of the yearly averaged sunspot number, dating from 1700 to present. The average sunspot number between 2016 January 1 and 2016 December 31 is indicated with a vertical dashed line. Roughly, 35 per cent of recorded years have a lower average sunspot number.

World Data Center 2023). The vertical line corresponds to the 2016–2017 average. Roughly, 35 per cent of recorded years have a lower average sunspot number. This implies that the inactive-region RVs may dominate solar RVs for roughly one third of the time.

5 INACTIVE-REGION RVS ARE NOT DOMINATED BY INSTRUMENTAL EFFECTS

It is in principle plausible that the variability shown in Fig. 4 at time-scales of around 2 d is due to the instrumental characteristics of the HARPS-N spectrograph, rather than genuine solar effects. To address this concern, we repeat our analysis with RVs from the NEID solar feed (Lin et al. 2022) taken between 2021 January 1 and 2022 June 13. We use RVs reported by version 1.1 of the NEID data reduction pipeline[2] and select observations that are free from known issues due to the daily wavelength calibration, a known cabling issue or evidence of poor observing conditions based on the pyrheliometer and exposure meter data. We select only observations taken before 17:30 and with airmass less than 2.25 to reduce calibration and atmospheric effects. Due to the different wavelength ranges and sensitivities of the NEID and HARPS-N spectrographs, the photometric shift, δRV_{phot}, and suppression of convective blueshift, δRV_{conv} (see Section 2.2), may have different contributions to the overall RVs. To account for this, following Milbourne et al. (2019), we fit a linear combination of these components to the NEID RVs.

It is worth noting that significant intra-day systematics appear in the NEID solar RVs due to, amongst other effects, unaccounted-for differential extinction. We model the sub-day variations with a best-fitting cubic trend to the 1-d phase-folded RVs, which we then subtract from the NEID solar RVs. While this is not as sophisticated as the treatment of Collier Cameron et al. (2019), we wish simply to recover the general variability properties seen in Fig. 4 and so a full treatment of NEID instrumental effects is both beyond the scope of this paper and not necessary for our purposes. As with the

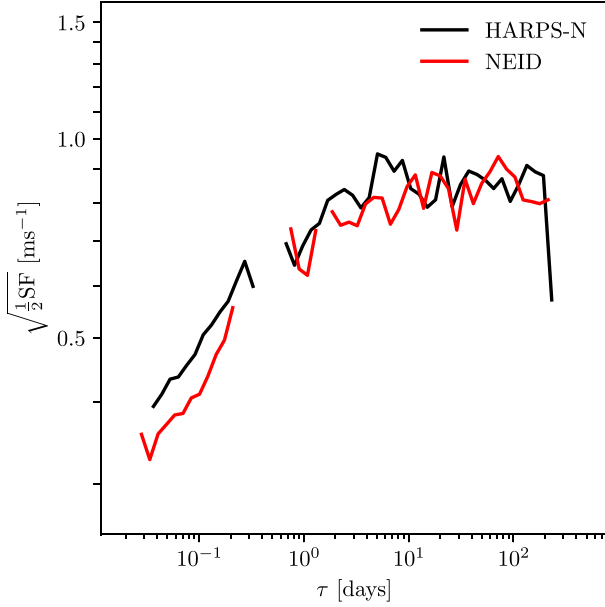[2]https://neid.ipac.caltech.edu/docs/NEID-DRP/index.html

Figure 7. SF comparison of inactive-region RVs calculated by subtracting the RV signatures of magnetically active regions (Section 2.2) from HARPS-N (black) and NEID (red) RVs between 2021 April 1 and 2021 November 12. Both SFs demonstrate similar variability characteristics despite the different spectrographs, indicating that the variation seen in the inactive-region RVs is predominately astrophysical in nature, not instrumental.

Figure 8. SF comparison of the inactive-region RVs (black), simulated oscillation, granulation, and supergranulation (OGS) RVs (pink), and the combined simulated RV time series (red). The simulated RVs show good agreement with the inactive-region RVs and indicate that supergranulation is a significant source of RV variability in the Sun, especially at time-scales longer than a few hours.

HARPS-N RVs, we use the recalculated *SDO*/HMI RVs and NEID RVs to produce a time series of inactive-region RVs. The HARPS-N and NEID RVs temporally overlap between 2021 April 1 and 2021 November 12 and we compare the HARPS-N- and NEID-derived inactive-region RV time series during this overlap to investigate the effects of instrumental systematics. Fig. 7 shows SFs of the two inactive-region RV series. We find that the variability of these two time series at all time-scales typically differs by less than 10 per cent, comparable to the lower bound sampling uncertainty we estimate in Appendix C2. This indicates that the results of Section 4 are genuine, and are not simply instrumental artefacts, and that any effects of instrumental differences are smaller than the intrinsic variability of the solar RVs; as such, we will focus the remainder of our analysis on the longer baseline time series of inactive-region RVs derived from HARPS-N. We note that this analysis qualitatively agrees with the results of Zhao et al. (2023), who compare solar RVs from state-of-the-art spectrographs, including HARPS-N and NEID. Those authors find remarkable agreement between the different instruments.

6 SUPERGRANULATION AS THE DRIVER OF INACTIVE-REGION RVS

In Section 4, we demonstrated that the inactive-region RVs have a roughly constant level of variability over the decline of solar cycle 24. To determine the cause of this variability, we compare the inactive-region RVs to a simulation of the oscillation, granulation, and supergranulation of a G2 star from Meunier & Lagrange (2019), based on the technique of Harvey (1984) and the results of Meunier et al. (2015). The simulated RV time series is averaged over 15 min to best match the HARPS-N observations.

Fig. 8 shows SFs of each component in the simulation of Meunier et al. (2019) (pink), the combined simulated time series (red), and the
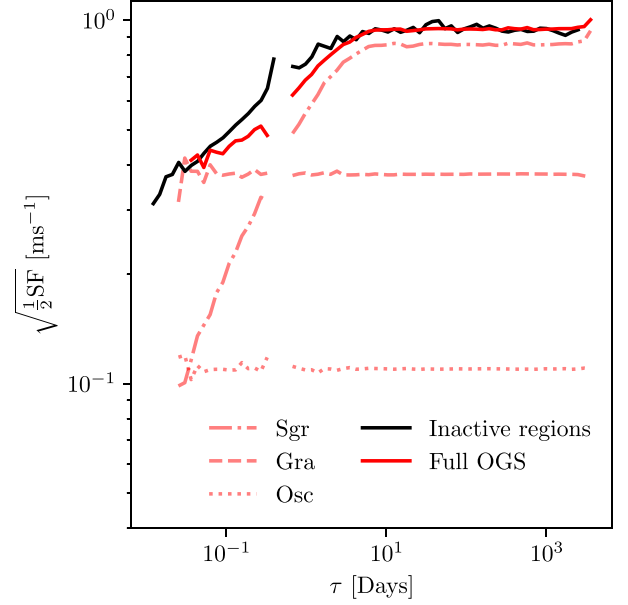
inactive-region RVs (black). The granulation (Gra) and supergranulation (Sgr) components are rescaled by a constant factor to match the observations; the oscillation (Osc) component is assumed to be negligible (e.g. Chaplin et al. 2019) and so is not rescaled. However, we opt to include the oscillation component for completeness. Since granulation and supergranulation dominate at different time-scales, we are able to rescale the simulated RVs to constrain the contribution of each process by matching the power in the inactive-region RVs at short and long time-scales, respectively. By combining and rescaling the simulated RVs in this way, we are able to accurately reproduce both the overall variability amplitude of the inactive-region RVs and the time-scale of the inactive-region RVs.

Meunier et al. (2019) found that the amplitude for the RV signals from granulation is 0.8 m s^{-1}, though there is evidence that an amplitude of 0.4 m s^{-1} is a more appropriate level (e.g. Sulis, Mary & Bigot 2020; Sulis et al. 2023). We see in Fig. 8 that the choice to use the lower level of granulation variability is justified; a granulation RV time series with RMS of 0.8 m s^{-1} would have more power at short time-scales than is seen in the true RVs. We find granulation and supergranulation variability amplitudes of 0.37 and 0.86 m s^{-1}, respectively. We therefore find a similar level of granulation to the lower level of Meunier & Lagrange (2020), and to the 0.33 m s^{-1} prediction of Dalal et al. (2023). We note that the 0.86 m s^{-1} level of supergranulation we find is around 25 per cent higher than the 0.68 m s^{-1} level found by Al Moulla et al. (2023), though the granulation amplitudes are similar. Given the difference in methodology between this work and that of Al Moulla et al. (2023), who use asteroseismology techniques to analyse Sun-as-a-star RVs from the HARPS and HARPS-N spectrographs, it is unsurprising that there is a difference in the exact amplitude of supergranulation derived. Both analyses demonstrate that supergranulation contributes a significant fraction of the total solar RV variability.

Our interpretation that the inactive-region RVs are primarily caused by granulation and supergranulation is supported by the fact that the level of variability is constant at various levels of the solar cycle (Figs 3 and 5). Muller et al. (2018) used images of the Sun from the Solar Optical Telescope as part of the HINODE synoptic programme (HINODE/SOT) between 2006 November and 2016 February to investigate photometric properties of solar granules. Over this period, they did not find changes in either the granulation contrast or granulation scale of the 3 per cent level at which they were sensitive, indicating no significant variation of granulation properties over the solar cycle.

We note that Fig. 8 does not include any instrumental systematics. While this makes it difficult to evaluate numerical uncertainties on the level of supergranulation quoted above, it is unlikely to significantly change the amplitude. First, a white noise profile (such as from photon noise) would inject power at all time-scales and appear flat as an SF. Since we constrain the granulation amplitude by using the short-time-scale power, we can be confident that we have not underestimated the uncorrelated noise. Thus, the rescaling we apply to the supergranulation time series to match the long-time-scale power is reasonably robust against the level of photon noise, which is estimated to be as low as 0.24 m s^{-1} (Al Moulla et al. 2023). Secondly, we show in Section 5 that the levels of variability of inactive-region RVs derived from HARPS-N and from NEID observations are consistent within typical sampling errors at all time-scales, indicating that the variability observed is not dominated by instrument-specific artefacts. This shows that the supergranulation amplitude derived from Fig. 8 is representative.

Fig. 8 shows that the combined simulated RVs show slightly reduced power on intermediate time-scales (between a few hours and a few days) as compared to the inactive-region RVs. Unaccounted-for correlated instrumental noise (e.g. an imperfect correction for differential extinction) could inject variability at intermediate time-scales to account for this discrepancy. Alternatively, the intrinsic variability spectrum of supergranulation may differ slightly from that of granulation. The simulations of Meunier et al. (2015) assume that supergranules evolve similarly to granules. The resulting simulated time series therefore share a common variability power law. A relaxation of this assumption may account for the mismatched power at intermediate time-scales. Additionally, the smallest scale active regions, unaccounted for in the model of Milbourne et al. (2019), may inject RV variability at these intermediate time-scales.

Regardless of the cause of this discrepancy, the agreement of the inactive-region RVs with both the amplitude and time-scale of the simulations of Meunier et al. (2019) and analysis of Al Moulla et al. (2023) offers good evidence that the variability seen in the inactive-region RVs is predominantly caused by supergranulation at time-scales of a few days and longer. Given that these RVs exhibit a relatively constant level of variability over the solar cycle (Figs 4 and 5), we provide evidence that supergranulation dominates the solar RVs on the approach to cycle 24 minimum and therefore poses a significant barrier to the detection of Earth twins whose Doppler shifts are ~ 0.1 m s^{-1}.

7 CONCLUSIONS

We have generated solar RVs from *SDO*/HMI images following the technique of Milbourne et al. (2019). The two components accounted for in this time series are the RV signatures arising from the suppression of convective blueshift in magnetically active regions and the effect of photometrically imbalanced regions transiting the rotating solar disc. We subtract these 'magnetic-activity' RVs from the disc-integrated RVs obtained from the HARPS-N solar feed to isolate the RV contribution from the magnetically quiet solar surface.

We find that the resulting 'inactive-region' RV time series shows no correlation with the well-known activity indicators log R'_{HK} and unsigned magnetic flux. This, combined with the reduced Fourier power at time-scales longer than roughly half a solar rotation period, shows that we are successful in removing the majority of the RV signal arising from the active regions on the Sun.

We show that the inactive-region RV variability is relatively stable, showing no significant change in level with either time or sunspot number. This contrasts starkly with the magnetic-activity RVs, which show a change in variability of more than an order of magnitude over the same baseline. This relative constancy in the inactive-region RV variability means that, when the Sun is relatively quiescent, the solar RVs are dominated by the RV signal originating in inactive regions, not active regions. We find that the two contributions are roughly even when the average sunspot number is around 40. This level of magnetic activity represents the 35th percentile recorded in archival sunspot data dating from 1700.

Finally, we compare the inactive-region RV time series to recent models of oscillation, granulation, and supergranulation (Meunier & Lagrange 2019). We find good agreement with both variability amplitude and time-scale between the inactive-region and simulated RV time series. We find that granulation and supergranulation induce RV variability with amplitudes of 0.37 and 0.86 m s^{-1}, respectively. In doing so, we provide empirical evidence that supergranulation can dominate solar RVs and therefore pose a significant barrier to detection of Earth twins. This is in agreement with the findings of Meunier et al. (2023).

honoured to be permitted to conduct astronomical research on Iolkam Duág (Kitt Peak), a mountain with particular significance to the Tohono Oódham.

DATA AVAILABILITY

This work is underpinned by the following publicly available data sets: *SDO*/HMI images, available at https://sdo.gsfc.nasa.gov/data/aiahmi/; and NEID solar RVs, made available at https://zenodo.org/record/7857521. In addition, this work makes extensive use of the HARPS-N solar RVs, which will be described and made available in an upcoming publication.

REFERENCES

Aigrain S., Pont F., Zucker S., 2012, MNRAS, 419, 3147
Al Moulla K., Dumusque X., Figueira P., Lo Curto G., Santos N. C., Wildi F., 2023, A&A, 669, A39
Barragán O., Aigrain S., Rajpaul V. M., Zicher N., 2022, MNRAS, 509, 866
Blunt S. et al., 2023, AJ, 166, 62
Boisse I., Bouchy F., Hébrard G., Bonfils X., Santos N., Vauclair S., 2011, A&A, 528, A4
Borucki W. J. et al., 2010, Science, 327, 977
Chaplin W. J., Cegla H. M., Watson C. A., Davies G. R., Ball W. H., 2019, AJ, 157, 163
Collier Cameron A. et al., 2019, MNRAS, 487, 1082
Crass J. et al., 2021, preprint (arXiv:2107.14291)
Dalal S., Haywood R. D., Mortier A., Chaplin W. J., Meunier N., 2023, MNRAS, 525, 3344
de Vries W. H., Becker R. H., White R. L., 2003, AJ, 126, 1217
Dumusque X., Boisse I., Santos N. C., 2014, ApJ, 796, 132
Dumusque X. et al., 2015, ApJ, 814, L21
Dumusque X. et al., 2021, A&A, 648, A103
Harvey J. W., 1984, in Noyes R. W., Rhodes E. J., Jr., eds. In probing the depths of star: the study of Solar oscillation from space, Vol. 327, Pasadena: JPL/NASA. Available at: https://scholar.google.com/scholar_lookup?title=Probing%20the%20Depths%20of%20a%20Star&publication_year=1984&author=J.%20Harvey
Haywood R. D. et al., 2014, MNRAS, 443, 2517
Haywood R. D. et al., 2016, MNRAS, 457, 3637
Haywood R. D. et al., 2022, ApJ, 935, 6
Hughes P. A., Aller H. D., Aller M. F., 1992, ApJ, 396, 469
Kjeldsen H. et al., 2005, ApJ, 635, 1281
Lakeland B. S., Naylor T., 2022, MNRAS, 514, 2736
Lin A. S. J. et al., 2022, AJ, 163, 184
Meunier N., Lagrange A. M., 2019, A&A, 625, L6
Meunier N., Lagrange A.-M., 2020, A&A, 642, A157
Meunier N., Desort M., Lagrange A. M., 2010a, A&A, 512, A39
Meunier N., Lagrange A. M., Desort M., 2010b, A&A, 519, A66
Meunier N., Lagrange A.-M., Borgniet S., Rieutord M., 2015, A&A, 583, A118
Meunier N., Lagrange A.-M., Boulet T., Borgniet S., 2019, A&A, 627, A56
Meunier N., Pous R., Sulis S., Mary D., Lagrange A.-M., 2023, A&A, 676, A82
Milbourne T. W. et al., 2019, ApJ, 874, 107
Muller R., Hanslmeier A., Utz D., Ichimoto K., 2018, A&A, 616, A87
Phillips D. F. et al., 2016, in Navarro R., Burge J. H., eds., Proc. SPIE Conf. Ser. Vol. 9912, Advances in Optical and Mechanical Technologies for Telescopes and Instrumentation II. SPIE, Bellingham, p. 99126Z
Rajpaul V., Aigrain S., Osborne M. A., Reece S., Roberts S., 2015, MNRAS, 452, 2269
Rajpaul V., Aigrain S., Roberts S., 2016, MNRAS, 456, L6
Rauer H. et al., 2014, Exp. Astron., 38, 249
Ricker G. R. et al., 2014, in Oschmann J. M. J., Clampin M., Fazio G. G., MacEwen H. A., eds, SPIE Conf. Ser. Vol. 9143, Space Telescopes and Instrumentation 2014: Optical, Infrared, and Millimeter Wave. SPIE, Bellingham, p. 914320
Saar S. H., Donahue R. A., 1997, ApJ, 485, 319
Sergison D. J., Naylor T., Littlefair S. P., Bell C. P. M., Williams C. D. H., 2020, MNRAS, 491, 5035
SILSO World Data Center, 2023, International Sunspot Number Monthly Bulletin and Online Catalogue, The International Sunspot Number. Royal Observatory of Belgium, avenue Circulaire 3, 1180 Brussels, Belgium. Available at: http://www.sidc.be/silso
Simonetti J. H., Cordes J. M., Heeschen D. S., 1985, ApJ, 296, 46
Sulis S., Mary D., Bigot L., 2020, A&A, 635, A146
Sulis S. et al., 2023, A&A, 670, A24
Zhao L. L. et al., 2023, AJ, 166, 173

APPENDIX A: A JUSTIFICATION THAT INTERPOLATION DOES NOT AFFECT THE RESULTS OF THIS PAPER

To match the high cadence of the HARPS-N solar RVs, we calculate RVs from the *SDO*/HMI images (see Section 2.2) every four hours, and interpolate these RVs on to the timestamps of the HARPS-N observations.

To assess the impact that interpolation has on the signal, we produce a month-long time series of RVs, generated from every available 720-s exposure set of *SDO*/HMI images from 2017 January 1 to 2017 February 1. From this high-cadence RV series, we produce a sub-sampled RV series with six RV measurements per day, to match the long-baseline series we use in the bulk of this paper. We then interpolate this sub-sampled RV series back on to the timestamps of the original high-cadence time series.

We find that the median absolute deviation between the high-cadence and interpolated RV series is 2.1 cm s^{-1}. This is significantly lower than any other level of variability we discus in this paper, justifying that our choice to interpolate the RVs calculated from the *SDO*/HMI images does not impact the results of this paper.

APPENDIX B: THE EFFECT OF SAMPLING NOISE ON THE RMS OF THE INACTIVE-REGION RVS

In Fig. 3, we see a variation in the RMS of inactive-region RV sub-series. While each RMS is calculated from a relatively large number of observations, we show in Fig. 4 that the inactive-region RVs become uncorrelated at time-scales longer than a few days. This relatively large time-scale, compared to the 50-d baseline of each sub-series, means that the sampling error on the RMS is larger than would be expected by simply considering the number of observations.

To test this, we take the simulated supergranulation time series of Meunier et al. (2019) and calculate the RMS for the same 50-d sub-series as in Fig. 3. This time series is constructed in a stationary manner, so that any variation seen between values of the RMS can with good confidence be attributed to sampling error. Fig. B1 shows the distribution of sub-series RMS values. As we are only interested
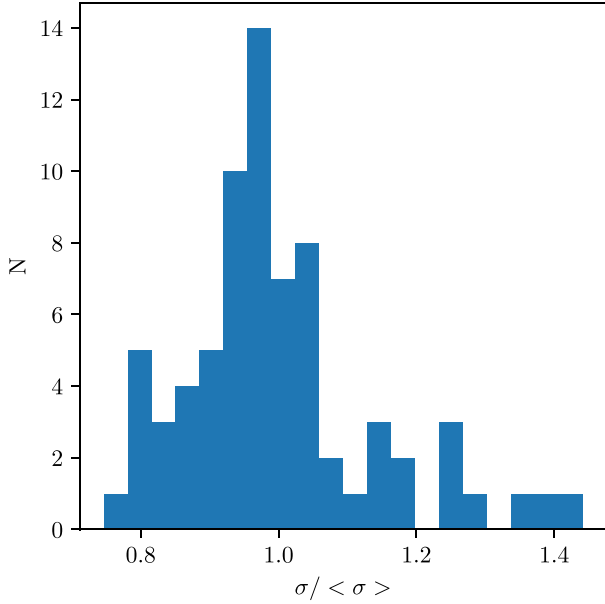
Figure B1. A histogram showing the distribution of RMS values of 50-d-long sub-series of the simulated supergranulation time series of Meunier et al. (2019). Since we are only concerned with the fractional scatter of the RMS measurements, we normalize the x-axis by the mean RMS value.

in the fractional difference between the individual RMS values, we normalize by the mean RMS. We see a relative scatter of the RMS values, $\sigma_\sigma/\langle\sigma\rangle$, of 14 per cent, where

$$\frac{\sigma_\sigma}{\langle\sigma\rangle} = \frac{\sqrt{\frac{1}{n_\sigma}\sum\left(\sigma - \left(\frac{1}{n_\sigma}\sum\sigma\right)\right)^2}}{\frac{1}{n_\sigma}\sum\sigma}. \tag{B1}$$

This value of $\sigma_\sigma/\langle\sigma\rangle$ is comparable to the inactive-region $\sigma_\sigma/\langle\sigma\rangle$ of 17 per cent. This indicates that the majority of the variation seen in Fig. 3 is due to statistical noise.

APPENDIX C: STRUCTURE FUNCTIONS

The SF is an analysis tool, which shows how the variability within a time series changes as a function of time-scale. It has had success in analysing photometric time series data (e.g. Hughes, Aller & Aller 1992; de Vries, Becker & White 2003; Sergison et al. 2020). SFs use a pairwise comparison of points in a time series $f(t)$ to calculate the level of variability as a function of time-scale. To calculate the variability of points with a given separation $\tau = |t_1 - t_2|$, we define the SF as

$$\mathrm{SF}(\tau) = \langle(f(t) - f(t + \tau))^2\rangle, \tag{C1}$$

where the angular brackets indicate an average over all pairs of observations with separation τ. In practice, SF is calculated for logarithmic bins in τ. That is to say, in the case of discrete data, the SF is calculated as

$$\mathrm{SF}(\tau_1, \tau_2) = \frac{1}{N_p}\sum_{ij}(f_i - f_j)^2, \tag{C2}$$

where the summation is taken over all pairs of data points, which are separated by $\tau_1 < |t_i - t_j| < \tau_2$, and N_p is the number of such pairs.

Fig. 7 of Sergison et al. (2020), reproduced here as Fig. C1, demonstrates the typical form of an SF. The short-time-scale plateau
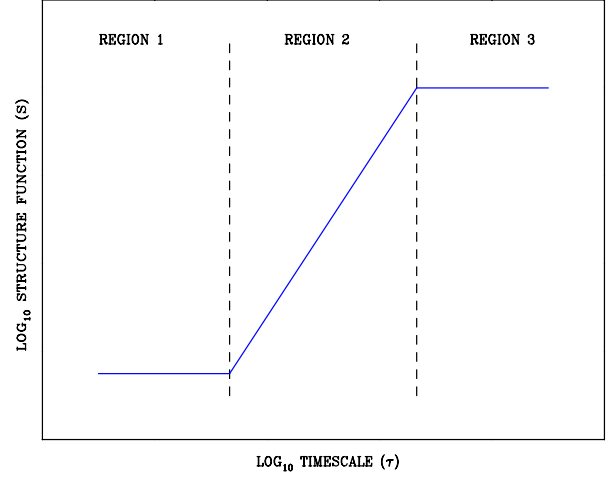

Figure C1. An illustration of the typical properties of SFs, reproduced from Sergison et al. (2020). Region 1 shows white noise present at short time-scales, often interpreted as instrumental noise. Region 2 shows a typical power-law relationship between time-scale and level of variability. Region 3 shows time-scales at which there is no further increase in variability. The transition between Regions 2 and 3 shows the characteristic time-scale of the variability.

shown in Region 1 indicates that any intrinsic variability in the signal is below the noise floor, so the variability is dominated by uncorrelated instrumental noise. In Region 2, there is a power-law increase in the SF, the gradient of which is determined by the spectrum of variability being investigated. Region 3 shows time-scales longer than the dominant variability time-scale in the data. Therefore, after this time-scale has been reached, the value of the SF stops increasing, again becoming uncorrelated. The transition between Regions 2 and 3, referred to as the 'knee', tells us the characteristic variability time-scale. Fig. 5 of Lakeland & Naylor (2022) demonstrates that, for a sinusoidal signal, the knee is at roughly a quarter of the period. This highlights that the time-scale identified by an SF, while related to any period present in a signal, is not the same as a period. Another feature of Fig. C1 is that the SF becomes larger as we move towards longer time-scales. While not strictly a cumulative measure, this behaviour is typical for most types of variability.[3] This property highlights how short-time-scale variations still impact the overall level of variability at longer time-scales.

An advantage of the SF over other analysis tools is the direct relationship between the SF and the level of variability at a given time-scale. We show in Appendix C1 that, for an uncorrelated signal, the SF will tend to the value $2\sigma^2$, where σ is the standard deviation of the data. This clear relationship between SF and standard deviation allows a much more direct interpretation of the level of variability within a signal for a given time-scale than, say, a Fourier PS.

For a more detailed description of some properties of SFs, see section 5 of Lakeland & Naylor (2022) and references therein. To avoid spurious results arising from bins with too few points, we require at least 100 pairs of observations in each τ bin throughout this paper.

---

[3]A notable exception is for periodic or quasi-periodic signals. For such signals, pairs of data points separated by multiples of the period will show little if any variation, causing characteristic dips in the SF.
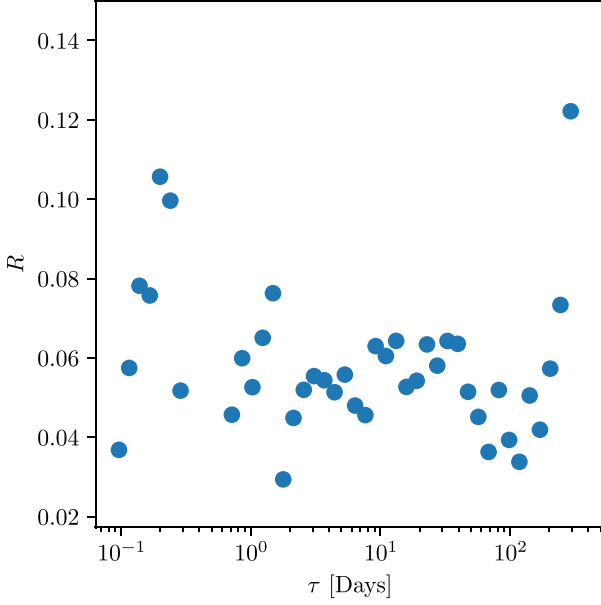
Figure C2. Ratio R of $\sigma_{\rm SF}$ to the median SF for 10 independent sub-series of the supergranulation RV time series discussed in Section 6.

C1 The relationship between the structure function and standard deviation

Consider an infinite, uncorrelated time series $f(t)$. This time series will have mean

$$\mu = \langle f(t) \rangle, \tag{C3}$$

and standard deviation

$$\sigma = \langle (f(t) - \mu)^2 \rangle. \tag{C4}$$

Since $f(t)$ is uncorrelated, we can also say that

$$\langle f(t) \times f(t+x) \rangle = \mu^2 + \sigma^2 \delta(x), \tag{C5}$$

where $\delta(x)$ is the δ-function. From equation (C1), it follows that

$$\mathrm{SF}(\tau) = \langle ((f(t) - \mu) - (f(t+\tau) - \mu))^2 \rangle \tag{C6}$$

$$= \left[\langle (f(t) - \mu)^2 \rangle + \langle (f(t+\tau) - \mu)^2 \rangle \right]$$
$$\quad -2\langle ((f(t) - \mu) \times (f(t+\tau) - \mu) \rangle \tag{C7}$$

$$= 2\sigma^2 - 2\left[\langle f(t) \times f(t+x) \rangle - \mu \langle f(t) \rangle - \mu \langle f(t+\tau) \rangle + \mu^2 \right]. \tag{C8}$$

From equation (C5), therefore we see that, for uncorrelated signals,

$$\mathrm{SF}(\tau) = 2\sigma^2. \tag{C9}$$

This is equivalent to equation (A4) of Simonetti et al. (1985).

C2 Estimating the effect of sampling noise

As discussed in appendix C of Sergison et al. (2020), it is non-trivial to estimate the effect of sampling noise on SF measurements [as we can think of $f(t)$ being drawn at random from an underlying distribution]. The difficulty arises in calculating the number of independent pairs of data points contributing to each measurement.

To estimate the level of sampling noise, we divide the simulated supergranulation RV time series of Meunier et al. (2019) (see Section 6) into year-long sub-series, and calculate the SF of each. This is in analogy to fig. 10 of Sergison et al. (2020). We opt to use the supergranulation time series as it will allow us to estimate the sampling noise at time-scales below and above the characteristic time-scale of the variability (as opposed to generating red-noise series as done by Sergison et al. 2020) and the time series is constructed to be stationary, so we can be confident that any variation between the SFs is due to the sampling noise.

Fig. C2 shows the ratio R of standard deviation of $\sqrt{\mathrm{SF}}$ to the median value of $\sqrt{\mathrm{SF}}$ at each time-scale. We show that the typical sampling error is of the order of 5 per cent of the median value of $\sqrt{\mathrm{SF}}$ at a given time-scale. Given that these sub-series are drawn from the same distribution, and that they are well sampled, we expect this to be a lower bound on the uncertainty associated with an SF measurement.

This paper has been typeset from a TEX/LATEX file prepared by the author.